L. Tillikainen, S. Siljamäki, H. Helminen, J. Alakuijala, and J. Pyyry. 2007. Determination of parameters for a multiple-source model of megavoltage photon beams using optimization methods. Physics in Medicine and Biology, volume 52, number 5, pages 1441-1467.

http://www.iop.org/journals/pmb
http://stacks.iop.org/pmb/52/1441

IOP PUBLISHING PHYSICS IN MEDICINE AND BIOLOGY

Phys. Med. Biol. **52** (2007) 1441–1467 doi:10.1088/0031-9155/52/5/015

Determination of parameters for a multiple-source model of megavoltage photon beams using optimization methods

L Tillikainen, S Siljamäki, H Helminen, J Alakuijala and J Pyyry

Varian Medical Systems Finland Oy, Paciuksenkatu 21, FIN-00270 Helsinki, Finland

E-mail: laura.tillikainen@varian.com

Received 19 September 2006, in final form 5 December 2006
Published 12 February 2007
Online at stacks.iop.org/PMB/52/1441

Abstract

Accurate modelling of the radiation output of a medical linear accelerator is important for radiotherapy treatment planning. The major challenge is the adjustment of the model to a specific treatment unit. One approach is to use a multiple-source model containing a set of physical parameters. In this work, the parameters were derived from standard beam data measurements using optimization methods. The source model used includes sub-sources for bremsstrahlung radiation from the target, extra-focal photon radiation and electron contamination. The cost function includes a gamma error measure between measurements and current dose calculations. The procedure was applied to six beam data sets (6 MV to 23 MV) measured with accelerators from three vendors, but the results focus primarily on Varian accelerators. The obtained average gamma error (1%, 1 mm) between dose calculations and measurements used in optimization was smaller than 0.7 for each studied treatment beam and field size, and a minimum of 83% of measurement points passed the $\gamma < 1$ criterion. For experiments made at different SSDs and for asymmetric fields, the average gamma errors were smaller than 1.1. For irregularly shaped MLC apertures, the differences in point doses were smaller than 1.0%. This work demonstrates that the source model parameters can be automatically derived from simple measurements using optimization methods. The developed procedure is applicable to a wide range of accelerators, and has an acceptable accuracy and processing time.

1. Introduction

Accurate dose calculation in radiotherapy treatment planning is necessary in order to achieve desired dose levels within the patient during treatment. The dose calculation can be divided into two separate tasks: the modelling of the radiation produced by the medical linear

accelerator (source modelling), and based on that, the calculation of the dose deposited in the patient. Any inaccuracies in the source modelling affect directly the calculated dose in the patient. Modern dose calculation algorithms such as superposition/convolution (Ahnesjö 1989, Mackie *et al* 1985, Mohan *et al* 1986, Boyer and Mok 1986) or Monte Carlo (Kawrakow *et al* 1996, Kawrakow 2000, Neuenschwander *et al* 1995) require a physics-based model of the accelerator output. Since individual machines—even of the same vendor and model—have slightly different physical characteristics, the source model should be flexible to allow adaptation to an individual treatment unit.

The proposed approaches for source modelling include full Monte Carlo (MC) simulation of the radiation transport through the accelerator head (Rogers *et al* 1995, Naqvi *et al* 2005), histogram-based models generated from the MC simulated phase space (Schach von Wittenau *et al* 1999, Chetty *et al* 2000, Fix *et al* 2004) and analytical models (Liu *et al* 1997b, Jiang *et al* 2001, Yang *et al* 2002, Fippel *et al* 2003, Ahnesjö *et al* 2005). These models differ in the amount of technical information required, their accuracy and their adaptability to different accelerators. Full MC simulation is very accurate, if all the necessary technical information is available. However, long simulation times are often required, and the adaptation of e.g. the electron beam energy and spot size (Sheikh-Bagheri and Rogers 2002b) to an individual treatment unit is a difficult and time-consuming process. The histograms created from the simulated phase space can potentially be more easily adjusted to an individual accelerator, but specific algorithms for this purpose have not yet been presented. Detailed information about the accelerator construction is still required to create the initial phase space.

Analytical source model approaches construct parameterized models of the photon and electron energy fluences and spectra. These models usually require only little technical information about the accelerator construction, but the functional forms describing the underlying physical phenomena should be carefully chosen. The parameters for the functions describing e.g. the energy fluence can be fitted to the MC simulated phase space or can be derived directly from measurements. Fitting of the functions to the MC simulated phase space (Liu *et al* 1997b) has the drawbacks mentioned above. Manual tuning of the parameters to fit measurements and dose calculations is non-trivial and time consuming, and hence automatic processes, such as the χ^2-minimization presented by Fippel *et al* (2003), are preferred. It is possible that the analytical models are not as accurate as fully MC-based models in all situations. If the parameters of the model are determined from measurements using optimization, the model may start to represent noise or measurement errors, and therefore will not generalize to other situations very well. These problems can possibly be alleviated by using a physics-based model and by applying some restrictions to the parameters during the optimization.

In this work, an automatic optimization procedure for the derivation of parameters for a multiple-source model from water-phantom measurements is presented. An attempt is made to carefully avoid measurement artefacts. Only the modelling of open beams and static MLC fields is covered in this work. Previously, the parameter derivation for the source models has not been studied extensively, even though it is essential for clinical use. A recent publication (Ahnesjö *et al* 2005) presents a semiautomatic process for parameter derivation. However, the work concentrated on the beam model and validation results, and the parameter derivation process was not discussed in detail. Some authors have, on the other hand, argued that it is very difficult or even impossible to deduce the parameters for a multiple-source model self-consistently from measurements in the presence of measurement artefacts (Naqvi *et al* 2005).

The multiple-source model used in this work was developed specifically to be used with the anisotropic analytical algorithm (AAA) in Eclipse™ Integrated Treatment Planning

Table 1. The free parameters of the multiple-source model that are modified during the optimization process.

Symbol	Unit	Description
$\bar{E}(r)$	MeV	Mean radial energy of primary photons (six discrete points)
$I(r)$	MeV m^{-2}	Intensity profile of primary photons (25 discrete points)
w_{ef}	–	The weight of the extra-focal photon source with respect to the primary photon source
σ_{ef}	mm	The width of the Gaussian intensity distribution for the extra-focal photon source
$\bar{E}_{\mathrm{ef}}$	MeV	The mean energy of the extra-focal photons
$\sigma_{\mathrm{e},i}$ $(i = 1, 2)$	mm	The widths of the Gaussians for the electron contamination energy fluence Φ_{e} in (3) defined at SAD
c	–	The weight for the first Gaussian convolution component for Φ_{e} in (3)
$w_{\mathrm{e},i}$ $(i = 1, \ldots, 6)$	–	The weights of the exponentials determining the electron contamination curve $c_{\mathrm{e}}(z)$ in (4)

System (Varian Medical Systems, Palo Alto, CA, USA), which is a superposition/convolution based algorithm utilizing MC-simulated pencil beam kernels. The source model is based on previously published models cited above, but it uses a specific set of free parameters that can be easily determined from measurements. In addition, the model includes a realistic characterization of the off-axis softening effect and a novel empirical model for electron contamination. Dosimetric evaluation of the AAA algorithm using the source model and parameter derivation process described here has already been performed for Varian treatment units at several clinics (Fogliata *et al* 2006, Van Esch *et al* 2006) using various test cases in water phantoms and heterogeneous phantoms. The optimization procedure has been found to be successful in reproducing the basic beam data with an overall accuracy of 3%, 1 mm in the build-up region and 1%, 1 mm elsewhere. In this work, a detailed description of the mathematical optimization methods is given, and verification of the procedure is performed using basic beam data for six treatment beams from three different vendors, and more complicated test cases (various SSDs, asymmetric fields, static MLC fields) for two Varian treatment beams.

2. Methods and materials

2.1. The multiple-source model of megavoltage photon beams

In this section, the multiple-source model used to describe the radiation output of the medical linear accelerator is presented. The free parameters of the model are summarized in table 1. These parameters are modified during the optimization process to minimize the deviations between measurements and dose calculations.

2.1.1. Primary photon source. The primary photon source models the bremsstrahlung radiation created in the metallic target as a result of the impinging electron beam. Primary photons in this text are defined as photons that have interacted only in the target before reaching the patient surface. Primary radiation is approximated with a point source located at the plane of the target, which is the same approach as used by Liu *et al* (1997b). The particle spectrum

of photons after the target, $S(E)$, has been simulated with the BEAMnrc (Rogers *et al* 1995) Monte Carlo code for each nominal energy. Realistic material and thickness information obtained for Varian accelerators were used in the simulation, and the electron beam energy was set to the accelerator nominal energy. The intensity distribution of the electron beam was a 2D Gaussian with a full width at half maximum (FWHM) value of 1.0 mm. Each energy component of the initial spectrum $S(E)$ is attenuated using the exponential attenuation law with the optimized thickness of flattening filter $d(r)$ at each radial distance. The flattening filter mass thickness $d(r)$ required to harden the initial spectrum is determined via an iterative process matching the mean energy of the attenuated spectrum to an optimized mean radial energy value $\bar{E}(r)$ at each radial distance. The discrete points defining the mean radial energy curve $\bar{E}(r)$ are free parameters in the model and are derived using the procedure described in section 2.3. This hardening procedure results in a radially dependent primary photon spectrum $S(E, r)$ below the flattening filter:

$$S(E, r) = S(E) \exp[-\mu/\rho(E)d(r)], \tag{1}$$

where $\mu/\rho(E)$ is the linear attenuation coefficient for energy E of the given flattening filter material (Hubbell and Seltzer 2004).

The energy fluence distribution of primary photons after the flattening filter can be slightly non-uniform. This phenomenon is taken into account in the proposed model with an intensity profile curve $I(r)$. It is discretized using 25 points, which are free parameters in the model. More points are placed in the large gradient areas than in small gradient areas of the profile. The primary energy fluence $\Phi_{\text{prim}}(x, y)$ at an arbitrary point (x, y) at SAD is then calculated in the following way:

$$\begin{aligned}\Phi_{\text{prim}}(x, y) = {} & I\left(\sqrt{x^2 + y^2}\right) \times F_{\text{X,top}}(x, y) \times F_{\text{X,bottom}}(x, y) \\ & \times F_{\text{Y,top}}(x, y) \times F_{\text{Y,bottom}}(x, y) \times F_{\text{MLC}}(x, y),\end{aligned} \tag{2}$$

where $F_{\text{i,top}}(x, y)$ and $F_{\text{i,top}}(x, y)$ $[i = X, Y]$ are the modulating functions for X- and Y-jaw top and bottom surfaces, respectively, and $F_{\text{MLC}}(x, y)$ is the modulating function for the multileaf collimator (MLC). If leakage through the beam limiting devices is not modelled, the modulating function is zero when the ray from target to the point (x, y) hits the corresponding beam limiting device, and unity otherwise. In the presented source model, the inter- and intra-leaf leakage through the MLC are not separately taken into account, but an overall MLC transmission, specific to the material and thickness of the MLC and to the beam nominal energy, is defined by the user. For rays that hit the MLC, $F_{\text{MLC}}(x, y)$ is set to this user-given transmission value. For static MLC fields, it would be possible to account for inter- and intra-leaf leakage by simply setting the values of $F_{\text{MLC}}(x, y)$ larger in the areas corresponding to leaf junctions than in the areas shadowed by the inner part of the leaves, but this effect is currently ignored. For dynamic MLC fields, however, this simplified approach would not be able to correctly model the tongue-and-groove effect. If one wishes to properly account for these effects, a more accurate modelling of the leaf shape and its movements needs to be applied.

2.1.2. Extra-focal photon source. The extra-focal photon radiation arises from interactions occurring in various parts of the accelerator head, primarily in the flattening filter, primary collimators and secondary jaws. In the proposed model the extra-focal radiation is modelled using a finite-size source located at the bottom surface of the flattening filter. This virtual source models all the photons that result from interactions occurring elsewhere than in the target. It is further assumed that the extra-focal radiation has a Gaussian intensity distribution. Because the extra-focal source is located below the target, the energy fluence distribution

below the last collimating device is wider compared to the primary source. The other effect is caused by the finite size of the source, which results in blurring near the edges of the fluence.

The extra-focal energy fluence at an arbitrary plane is computed in the following way. For each pixel in the destination fluence array, the contributions from each element of the finite source are added. The contribution is zero (or equal to user-given MLC transmission value), if the ray from the source element to the destination element hits the X- or Y-jaws or the MLC leaves, and one otherwise. This modulation is similar to that presented in (2) for the calculation of primary energy fluence. In addition, the contribution is scaled by the Gaussian weight of the source element, by the inverse square of the distance between the elements at the source and destination planes, and by the cosine of the angle of the ray with respect to central axis.

The extra-focal source model includes an empirically derived spectrum, whose energy axis is scaled in order to obtain a given mean energy $\bar{E}_{\mathrm{ef}}$. Off-axis variation in the extra-focal source spectrum is not modelled. The weight of the extra-focal source with respect to the primary photon source w_{ef}, the width of the Gaussian at the source plane σ_{ef} and the mean energy $\bar{E}_{\mathrm{ef}}$ are free parameters in the model and are derived using the process described in section 2.3. The weight w_{ef} is defined as the ratio of the extra-focal energy fluence to primary energy fluence in air at isocentre, if both sources were point sources. The distance from the target to the extra-focal source and the distances from target to each collimating device must be set according to the machine geometry, and these values are not changed during the optimization process.

2.1.3. Electron contamination source. The energy fluence of contaminant electrons Φ_{e} is calculated in the proposed model as a linear combination of two convolution terms:

$$\Phi_{\mathrm{e}}(x, y) = c\Phi_{\mathrm{prim}}(x, y) \otimes G_1(x, y) + (1 - c)\Phi_{\mathrm{prim}}(x, y) \otimes G_2(x, y) \tag{3}$$

where $\Phi_{\mathrm{prim}}(x, y)$ is the primary energy fluence defined in (2), and G_i is a Gaussian kernel with width $\sigma_{\mathrm{e},i}$ ($i = 1, 2$), and $\otimes$ is the convolution operator. The widths of the Gaussians, $\sigma_{\mathrm{e},1}$ and $\sigma_{\mathrm{e},2}$, as well as their relative weights, c and $1 - c$, are free parameters in the model. The width parameters $\sigma_{\mathrm{e,i}}$ ($i = 1, 2$) are defined at SAD and are scaled to the distance at which the dose is calculated. Therefore, the electron contamination source can be understood as a finite-size source located at the plane of the target.

The total energy deposited by the contaminant electrons as a function of depth is modelled by an empirical curve $c_{\mathrm{e}}(z)$, which is determined from the difference between the measured depth dose curve (PDD) and calculated PDD without contaminant electrons for the largest field size $\delta_{\mathrm{MaxFS}}(z)$. The electron contamination curve $c_{\mathrm{e}}(z)$ is modelled as a linear combination of six exponentials:

$$c_{\mathrm{e}}(z) = \sum_{i=1}^{6} w_{\mathrm{e},i} \exp(-k_i z), \tag{4}$$

where the attenuation coefficients k_i ($i = 1, \ldots, 6$) are fixed to 0.04, 0.10, 0.18, 0.27, 0.35 and 0.45 mm^{-1}, and $w_{\mathrm{e},i}$ are free parameters derived using the procedure described in section 2.3.4. This model was chosen since it provided a good fit to the difference curve $\delta_{\mathrm{MaxFS}}(z)$. The width parameters $\sigma_{\mathrm{e,i}}$ ($i = 1, 2$) also effectively model the field size dependence in the electron contamination dose, since the width of the primary energy fluence to be convolved with the Gaussians varies with field size.

2.2. Dose calculation methods

2.2.1. The anisotropic analytical algorithm for volume dose calculation. The anisotropic analytical algorithm (AAA) is a superposition/convolution-based volumetric dose calculation method implemented to Eclipse™ Integrated Treatment Planning System. AAA dose deposition is based on the algorithm originally developed by Ulmer *et al* (Ulmer and Harder 1995, 1996, Ulmer *et al* 2005), but the Gaussian functions have been replaced by exponential functions to better model the scatter near the borders of lateral heterogeneities. Although the complete description of the dose deposition mechanisms used in AAA is a subject of separate communication, for completeness, the basic principles of the AAA algorithm in homogeneous water medium are outlined below.

In AAA volumetric dose calculation ($M_{\text{v.d.}}$), the clinical beam is divided into small beamlets β and the patient body is divided into a 3D matrix of divergent calculation voxels along these beamlets. A user-given calculation grid parameter ($2, \ldots, 5$ mm) determines the size of the calculation voxels and beamlets. The final dose is calculated as a superposition of the doses deposited by primary photons, extra-focal photons and contaminant electrons. The primary and extra-focal photon components are calculated with the same principle, but they have separate scatter kernels and energy fluences.

A set of monoenergetic pencil beam kernels $K(r, z, E)$ (J MeV^{-1} m^{-3}) was simulated using the DOSRZnrc user code of EGSnrc (Kawrakow 2000) for energies $E = 0.25, \ldots,$ 25 MeV to be used in $M_{\text{v.d.}}$. The energy spacing was 0.25 MeV for energies smaller than 4 MeV and 0.5 MeV for energies larger than 4 MeV. Photon interaction forcing was used for the first interaction as a variance reduction technique. The radius of the impinging monoenergetic photon beam was set to 0.1 mm. The total number of particles for each monoenergetic pencil beam was 50 million. The voxel sizes in r- and z-directions were 1.0 mm below 50 mm and 2.5 mm above 50 mm for both directions.

For every beamlet β, a polyenergetic pencil beam kernel $K_\beta(r, p_z)$ is constructed for every voxel p_z along the fanline. The kernel $K_\beta(r, p_z)$ is computed as a superposition of the monoenergetic kernels $K(r, z, E)$ weighted with the spectrum of the beamlet (i.e. $S(E, r)$ for the primary photons). Then the energy deposition is separated into depth-directed (along the fanline) and lateral (perpendicular to the fanline) components. The depth-dependent component I_β takes into account the total energy deposited in the layer p_z:

$$I_\beta(p_z) = \Phi_\beta \iint K_\beta(r, p_z) r \, \mathrm{d}r \, \mathrm{d}\theta \ \ (\mathrm{J\ m^{-2}}), \tag{5}$$

where θ is the azimuthal coordinate of the cylindrical geometry of the pencil beam, and Φ_β is the photon fluence (primary or extra-focal) of beamlet β, which is assumed to be uniform over the beamlet cross-section. The lateral component $k_\beta(\theta, \lambda, p_z)$ is modelled as a superposition of six radial exponential functions:

$$k_\beta(\theta, \lambda, p_z) = \sum_{i=1}^{6} c_i \frac{1}{\lambda} \exp(-\mu_i \lambda) \ \ (\mathrm{m^{-1}}). \tag{6}$$

For each depth p_z and angle θ, this component describes the fraction of energy deposited into an infinitesimally small angular section at a distance λ to the beamlet central axis. The attenuation coefficients μ_i in (6) are fixed, and are chosen such that the effective ranges $1/\mu_i$ vary in between $0, \ldots, 200$ mm. The weight parameters c_i are fitted for each calculation plane to minimize deviations between the analytical kernel presentation in (6) and the poly-energetic kernel computed from the monoenergetic pre-calculated pencil beam kernels. The analytic expression for $k_\beta(\theta, \lambda, p_z)$ is necessary for the heterogeneity correction method in AAA, which takes into account the varying local electron density. However, the heterogeneity

correction method is not described here, since only water phantom calculations are used in this work.

For a homogeneous phantom, the energy deposited by a single beamlet β into an arbitrary point p in plane p_z is calculated as

$$E_\beta(p) = I_\beta(p_z) \times k_\beta(\theta, \lambda, p_z) \ (\mathrm{J\,m^{-3}}). \tag{7}$$

For the electron contamination, the energy contribution is calculated without taking the lateral scatter in the phantom into account:

$$E_{\beta,\mathrm{e}}(p) = \Phi_{\beta,\mathrm{e}} \times c_\mathrm{e}(p_z) \ (\mathrm{J\,m^{-3}}), \tag{8}$$

where $\Phi_{\beta,\mathrm{e}}$ is the electron contamination energy fluence for beamlet β in plane p_z and $c_\mathrm{e}(p_z)$ is the electron contamination curve defined in section 2.1.3 in plane p_z. The total energy deposited in an arbitrary point p is the superposition of the contributions from individual beamlets. Finally, the energy distribution is converted to dose distribution by dividing with the local mass density.

2.2.2. Pencil-beam-kernel based point dose calculation. In the proposed optimization procedure, the dose must be calculated hundreds of times during the process for many field sizes. Using $M_{\mathrm{v.d.}}$ the process would take approximately 170 h on an Intel Xeon 3.06 GHz level computer with two processors and 2 GB of RAM. Therefore, a fast point dose calculation algorithm ($M_{\mathrm{p.d.}}$) capable of calculating photon dose in a water phantom to a given set of calculation points was developed. It is based on the superposition of Monte Carlo calculated pencil beam kernels $K(r, z, E)$ defined in section 2.2.1, and is roughly three orders of magnitude faster than $M_{\mathrm{v.d.}}$. The purpose of $M_{\mathrm{p.d.}}$ is to approximate the actual calculation method $M_{\mathrm{v.d.}}$, but absolute agreement is not required since the difference between the two methods is taken properly into account during the process.

In this section, the algorithm to calculate the energy density $E(i)$ ($\mathrm{J\,m^{-3}}$) at point i deposited by the primary and extra-focal photons is presented. The corresponding dose $d(i)$ (Gy) can be obtained by dividing $E(i)$ with the mass density $\rho(i)$ ($\mathrm{kg\,m^{-3}}$) of the corresponding calculation voxel. In the developed algorithm, a spherical, divergent grid is created around a given calculation point $i = (x, y, z)$. The grid spacing increases as a function of square root of the distance from point i, being 1 mm close to the point i and approximately 15 mm near the field edge. A divergent grid was used instead of an equally spaced Cartesian grid, since the dose values in the pencil beam kernel drop fast when the distance from the pencil beam central axis increases.

A pencil beam is assumed to traverse from a point source representing the target across the centre of each grid point. The distance z_j from phantom surface along the pencil beam to the grid point j and the closest (perpendicular) distance r_j between the ray representing the pencil beam and the calculation point are computed to determine the contribution of the corresponding pencil beam to the primary photon energy density. The total energy density deposited by primary photons to the calculation point $E_{\mathrm{prim}}(i)$ is obtained as the superposition of the contributions from all grid points j and from all monoenergetic beams. The weight for each monoenergetic beam is determined from the corresponding photon energy spectrum component $S(j, k)$. Each grid point has a separate photon spectrum due to the off-axis softening effect. The individual dose depositions are further scaled by the corresponding area $A(j)$ of the grid element projected to the isocentre plane and by the intensity profile value $I(j)$ at the projection point. The pencil beam kernels must also be divided by the energy of

the impinging pencil beam so that the total energy deposited is the same for each pencil beam. The following formula summarizes the calculation of the $E_{\mathrm{prim}}(i)$:

$$E_{\mathrm{prim}}(i) = \sum_{j=1}^{N(i)} \sum_{k=1}^{M} S(j,k)A(j)I(j)[K(r_j, z_j, E_k)/E_k]\Delta E_k \ (\mathrm{J\,m^{-3}}), \tag{9}$$

where $N(i)$ is the number of grid points for calculation point i, M is the number of energy bins, $S(j,k)$ (unitless) is the energy spectrum component for energy bin k and grid point j, $A(j)$ ($\mathrm{m^2}$) is the grid element area at isocentre plane, $I(j)$ ($\mathrm{MeV\,m^{-2}}$) is the intensity profile value at grid point j, $K(r_j, z_j, E_k)$ ($\mathrm{J\ MeV^{-1}\,m^{-3}}$) is the pencil beam kernel and ΔE_k (MeV) is the size of kth energy bin. The energy deposited by the extra-focal photons $E_{\mathrm{ef}}(i)$ is calculated in a similar way to primary photons, but $I(j)$ is replaced by the extra-focal energy fluence $\Phi_{\mathrm{ef}}(j)$ and $S(j,k)$ by the extra-focal photon spectrum $S_{\mathrm{ef}}(k)$ (same units).

During the optimization, the set of measurement points remains constant. Therefore, it is possible to transform the energy deposition calculation for a single calculation point into a matrix multiplication for a set of K points:

$$\underset{K\times 1}{\boldsymbol{e}} = \underset{K\times ML}{\boldsymbol{A}_{\mathrm{prim}}} \times \underset{ML\times 1}{\boldsymbol{s}_{\mathrm{prim}}} + w_{\mathrm{ef}} \underset{K\times M}{\boldsymbol{A}_{\mathrm{ef}}} \times \underset{M\times 1}{\boldsymbol{s}_{\mathrm{ef}}}, \tag{10}$$

where $\boldsymbol{e}$ is the calculated energy density for the K points, $\boldsymbol{s}_{\mathrm{prim}}$ a combined spectrum and intensity vector, $\boldsymbol{s}_{\mathrm{ef}}$ is the extra-focal spectrum vector, $\boldsymbol{A}_{\mathrm{prim}}$ and $\boldsymbol{A}_{\mathrm{ef}}$ are the primary and the extra-focal energy deposition matrices, respectively, K is the number of measurement points and L is the number of radial bins. Vector $\boldsymbol{s}_{\mathrm{prim}}$ contains the radial spectrum components $S(E,r)$ at discrete radii ρ_l and at discrete energy bins E_k multiplied by the intensity profile values $I(r)$ at discrete radii. The extra-focal spectrum vector $\boldsymbol{s}_{\mathrm{ef}}$ is composed of the extra-focal photon spectrum components at discrete energy bins E_k. The matrix $\boldsymbol{A}_{\mathrm{prim}}$ is calculated by scoring the term $A(j)K(r_j, z_j, E_k)/E_k$ in (9) into the correct position of the matrix on the basis of the coordinates of the grid point j and energy E_k. The individual depositions are linearly divided between corresponding two cells of the matrix. The extra-focal energy deposition matrix $\boldsymbol{A}_{\mathrm{ef}}$ is obtained in a similar manner by scoring the term $A(j)\Phi_{\mathrm{ef}}(j)K(r_j, z_j, E_k)/E_k$ into the matrix.

2.2.3. Absolute dose calculation. The increase in output factors as a function of increasing field size is caused by three factors: increased phantom scatter, increased head scatter (extra-focal radiation) and decreased backscattered radiation (Liu *et al* 1997a). In this work, the backscatter is modelled using field-size dependent collimator backscatter factors (CBSF), which are determined from a set of output factors (OF) measured for rectangular, symmetric fields. It is assumed that the effects of phantom scatter and extra-focal radiation are modelled accurately by the dose calculation method and multiple-source model used. The missing increase in the radiation output is assumed to be caused by collimator backscatter. Dependence on the off-axis location of the jaw opening is not modelled. This approximation is supported by the findings of Liu *et al* (2000) that were based on detailed MC simulations. The collimator backscatter factor for jaw position (X_1, X_2, Y_1, Y_2) is computed as

$$\mathrm{CBSF}(X,Y) = [\mathrm{OF}_{\mathrm{ref}} \times D(X,Y)]/[\mathrm{OF}(X,Y) \times D_{\mathrm{ref}}], \tag{11}$$

where $X = X_2 - X_1$, $Y = Y_2 - Y_1$, $\mathrm{OF}_{\mathrm{ref}}$ is the measured output factor value for the reference field, $\mathrm{OF}(X,Y)$ is the measured output factor value for field size $X \times Y$, D_{ref} is the calculated dose (without backscatter) for the reference field and $D(X,Y)$ is the calculated dose (without backscatter) for field size $X \times Y$. The reference field is a centrally centred 100×100 $\mathrm{mm^2}$ field. The same depth, e.g. 50 mm, is used for all the measurements and calculations in (11).

During forward dose calculation, the CBSF value for an arbitrarily shaped field is interpolated from the pre-calculated CBSF table based on the current jaw positions (X_1, X_2, Y_1, Y_2).

In order to calculate the monitor units for an arbitrary field, information is required about the machine calibration in reference conditions (calibration geometry). For example, the treatment machine could have been calibrated such that 100 monitor units correspond to 1 gray at 100 mm depth for a 100×100 mm^2 field in an isocentric setup. The number of monitor units for an arbitrary field is then calculated as

$$\mathrm{MU}_{\mathrm{calc}} = \mathrm{CBSF}(X, Y)(\mathrm{MU/Gy})_{\mathrm{calib}}(D_{\mathrm{calib}}/D_{\mathrm{calc}})\mathrm{Gy}_{\mathrm{pre}}, \tag{12}$$

where $\mathrm{MU}_{\mathrm{calc}}$ is the calculated number of monitor units, $\mathrm{CBSF}(X, Y)$ is the collimator backscatter factor, $(\mathrm{MU/Gy})_{\mathrm{calib}}$ is the measured number of monitor units per unit dose in the calibration geometry, D_{calib} is the calculated dose at the calibration geometry, D_{calc} is the calculated dose at the dose prescription point in the field and $\mathrm{Gy}_{\mathrm{pre}}$ is the prescribed dose (Gy) for the prescription point.

2.3. The optimization procedure for parameter derivation

The proposed automatic optimization procedure is based on the minimization of an objective function measuring the deviation between dose calculations and measurements. To obtain acceptable calculation times, a fast point dose calculation method ($M_{\mathrm{p.d.}}$) presented in section 2.2.2 is used during the optimization instead of the volumetric calculation method ($M_{\mathrm{v.d.}}$) presented in section 2.2.1. Since $M_{\mathrm{p.d.}}$ is only capable of calculating the photon dose, $M_{\mathrm{v.d.}}$ is still used to derive the electron contamination parameters. The procedure consists of the following phases:

(i) Resampling, adjustment and scaling of the measured beam data.
(ii) Initial optimization of photon parameters $\bar{E}(r)$, $I(r)$, σ_{ef}, w_{ef} and $\bar{E}_{\mathrm{ef}}$ using Powell's direction search method. The measurements in the build-up region are ignored in this phase.
(iii) Optimization of the electron contamination parameters $\sigma_{\mathrm{e},1}$, $\sigma_{\mathrm{e},2}$, c, and the weights $w_{\mathrm{e},i}$ $(i = 1, \ldots, 6)$ for $c_{\mathrm{e}}(z)$ based on the differences between the measured PDDs and calculated PDDs without electron contamination.
(iv) To allow the use of $M_{\mathrm{p.d.}}$ also in the build-up region, the differences between $M_{\mathrm{p.d.}}$ and $M_{\mathrm{v.d.}}$ are evaluated at the current parameter values. The differences are mostly due to the inability of $M_{\mathrm{p.d.}}$ to calculate the electron dose. The measured beam data, which are used as an optimization target, are replaced by the original measurements subtracted by the differences.
(v) Refining the optimization based on the modified measurement data to take the measurements in the build-up region into account.

The optimization process is not sensitive to the initial parameter values used in step (ii), which is demonstrated with an example case in section 3.1. In the following sections the above steps are described in more detail.

2.3.1. Processing of measurements. The measurement set used in the optimization process includes percentage depth dose curves (several field sizes), lateral profiles (several depths) and diagonal profiles (several depths for the largest field size). For example, field sizes of 30×30, 40×40, 70×70, 100×100, 200×200 and 400×400 mm^2 and depths of d_{max}, 50, 100, 200 and 300 mm can be used.

Before the actual optimization, the measurements are checked for some potential inconsistencies. If it is possible, the erroneous measurements are corrected—otherwise they

are discarded from the optimization. This is done to avoid the characterization of measurement errors in the model. Asymmetric profiles are not necessarily an error in the measurements, since the treatment beam can sometimes be slightly asymmetric. However, since the source model used is symmetric, symmetrization of profiles is beneficial for the optimization. The adjustments made to measurements are described in the following list:

- Lateral shift of the profiles to make the 50% dose values of both profile sides to lie at a position equally far from the central axis. If only one profile side is measured, the profile is shifted such that the 50% dose value is at the expected position.
- Averaging of the profile sides to make the beam data symmetric.
- Removal of points in the profile located further than a threshold distance of 70 mm from the field edge to avoid the dominance of profile tail region in the objective function.
- Checking for missing lateral scatter due to the limited size of the water phantom (some points measured too close to the edge of the phantom). If such an error is detected, the corresponding profile is discarded from the optimization.
- Removal of values that saturate into an unphysical constant value, caused by e.g. the detector hitting the phantom wall.

The calculated PDD for each field size is scaled with respect to the measured PDD by a factor which minimizes the squared error between the curves excluding the build-up region. For profiles, a separate scaling factor is determined for each curve from the least-squares fit between measurements and calculations in the inner beam region.

2.3.2. Objective function. The problem of determining the photon parameters for the multiple-source model can be reformulated as a problem of minimizing an objective function $f(\boldsymbol{x})$, which is a measure of the agreement between a set of K measurement points $\boldsymbol{D}^{\mathrm{m}}$ ($K = 5000, \ldots, 10\,000$) and a set of K dose values calculated with the point dose algorithm $\boldsymbol{D}^{\mathrm{c}}(\boldsymbol{x})$. The parameter set $\boldsymbol{x}$ to be optimized consists of the discretized $\bar{E}(r)$ and $I(r)$ curves, and of the extra-focal source parameters σ_{ef}, $\bar{E}_{\mathrm{ef}}$ and w_{ef} (see table 1). The electron contamination parameters $w_{\mathrm{e},i}$, $\sigma_{\mathrm{e,i}}$ and c (see table 1) are determined using a different technique described in section 2.3.4. The objective function was chosen to be the product of a penalty term $f_{\mathrm{penalty}}(\boldsymbol{x})$ and a gamma error term $\hat{\gamma}$:

$$f(\boldsymbol{x}) = f_{\mathrm{penalty}}(\boldsymbol{x}) \times \sum_{i=1}^{K} w_i \hat{\gamma}\left(\boldsymbol{D}^{\mathrm{c}}(\boldsymbol{x}), D_i^{\mathrm{m}}\right), \tag{13}$$

where w_i is a weighting factor for point i. The modified gamma $\hat{\gamma}$ in (13) is defined as

$$\hat{\gamma}(\cdot) = 3\gamma^2(\cdot) + \gamma(\cdot), \tag{14}$$

where $(\cdot)$ stands for the arguments shown in (13) and $\gamma(\cdot)$ is the gamma error norm (Low *et al* 1998) with the dependence on the calculated curve denoted explicitly in the argument. The heuristic penalty term $f_{\mathrm{penalty}}(\boldsymbol{x})$ is defined as

$$f_{\mathrm{penalty}}(\boldsymbol{x}) = g(p_E(\boldsymbol{x}), p_I(\boldsymbol{x}), p_{\mathrm{ef}}(\boldsymbol{x})), \tag{15}$$

where $g(\cdot)$ is a monotonically increasing function of all arguments, and $p_E(\boldsymbol{x})$, $p_I(\boldsymbol{x})$ and $p_{\mathrm{ef}}(\boldsymbol{x})$ are penalty terms for mean radial energy, intensity profile and extra-focal source parameters, respectively. The process is not sensitive to the functional form of $g(\cdot)$. The penalty term $p_E(\boldsymbol{x})$ is computed as a squared sum of terms penalizing for unphysical radially increasing mean energy and a term penalizing for a noisy curve. The penalty term $p_I(\boldsymbol{x})$ contains a similar term to penalize for noise, added with a term constraining the shape of the intensity profile to avoid unphysical shapes, like increasing intensity outside field edge. The

penalty factor $p_{\mathrm{ef}}(\boldsymbol{x})$ includes quadratic terms penalizing for deviations from certain reference values with a small weight.

The gamma error norm, which is a measure of the distance between a measurement point and a calculated curve in a dose–distance scale, was used as a distance measure to have a uniform error measure both in high and low gradient regions of the dose distributions. The rationale of using the modified gamma function ($\hat{\gamma}$) defined in (14) instead of the standard gamma function is the following. The quadratic term ($3\gamma^2$) penalizes more for large deviations between measurements and calculations than the linear term (γ) and hence reduces the maximum deviations. The linear term (γ) is used to have a larger gradient near the optimum location and hence to better guide the optimization into the correct direction. A gamma error value is calculated separately for each measurement point in the PDDs, profiles and diagonal profiles for each field size. The weighted sum of the errors is calculated, where each field size, curve and point in the curve can be weighted differently. Value $w_i = 2$ was used for PDDs and diagonal profiles, and value $w_i = 1$ for lateral profiles. During the first phase of the optimization, the weights for the points located in the build-up region are further set to zero as described earlier.

2.3.3. Optimization of photon parameters. Optimization techniques utilizing the gradient of the objective function are commonly used and often converge very fast. However, the analytical calculation of the gradient of the objective function in (13) is difficult. Numerical calculation of the gradient is possible, but it is computationally expensive for the current problem, since for each parameter in the set $\boldsymbol{x}$, all the beam data need to be calculated at least twice. Therefore, Powell's direction search method (Powell 1965), which is not based on gradient information, was chosen as the optimization method. As nearly all optimization techniques, it is not guaranteed to find the global minimum. However, since (13) is nearly quadratic and heuristic penalty terms are used, multiple local minima are unlikely to occur in practice.

In Powell's direction search, an initial starting point $\boldsymbol{x}_0$ is first chosen. Then during each iteration, the function $f(\boldsymbol{x})$ is minimized separately along n linearly independent directions $\boldsymbol{\xi}_1, \boldsymbol{\xi}_2, \ldots, \boldsymbol{\xi}_n$. The parameter vector $\boldsymbol{x}_i$ after the line minimization along ith direction ($i = 1, \ldots, n$) is calculated as (Powell 1965):

$$\boldsymbol{x}_i = \boldsymbol{x}_{i-1} + \lambda_i \boldsymbol{\xi}_i, \tag{16}$$

where $\boldsymbol{x}_{i-1}$ is the parameter vector after the previous line minimization and λ_i is selected such that $f(\boldsymbol{x}_{i-1} + \lambda_i \boldsymbol{\xi}_i)$ is the minimum along direction $\boldsymbol{\xi}_i$. The initial search directions $\boldsymbol{\xi}_i$ can be chosen to be equal to the coordinate directions. After n line minimizations, a new conjugate direction $\boldsymbol{\xi}_{\mathrm{conj}}$ is computed as (Powell 1965):

$$\boldsymbol{\xi}_{\mathrm{conj}} = (\boldsymbol{x}_n - \boldsymbol{x}_0)/\|\boldsymbol{x}_n - \boldsymbol{x}_0\|_2, \tag{17}$$

where $\boldsymbol{x}_0$ is the starting point for the current iteration, and $\boldsymbol{x}_n$ is the parameter vector after nth line minimization. If $\boldsymbol{\xi}_{\mathrm{conj}}$ is evaluated as a good direction (based on the linear independence of the resulting set of directions), one of the existing directions is replaced by $\boldsymbol{\xi}_{\mathrm{conj}}$ and one more line minimization is performed along $\boldsymbol{\xi}_{\mathrm{conj}}$. The above process is iterated until some stopping criteria are reached. In this work, the minimum change in the objective function value was used as a stopping criterion.

A one-dimensional line minimization algorithm is required in Powell's method to determine λ_i. In the proposed implementation, the golden section search is used during the first iteration, when changes in the parameter values are large, and parabolic interpolation is used during the subsequent iterations to avoid large numbers of function evaluations. The

golden section search is a standard technique for finding the minimum of a one-dimensional function by successively narrowing the upper and lower bounds for the minimum point (Press *et al* 1999).

2.3.4. Optimization of electron contamination parameters. The empirical electron contamination curve $c_e(z)$ is determined from the difference curve $\delta_{MaxFS}(z)$ between the measured PDD and the calculated PDD without electron contamination for the largest field size. To obtain the weights $w_{e,i}$ that define the electron contamination curve in (4), electron PDDs corresponding to each exponential component $c_e(z) = \exp(-k_i z)$ are calculated with $M_{v.d.}$ for the largest field size. Then a least-squares fit between the calculated PDDs and the difference curve $\delta_{MaxFS}(z)$ is performed to yield the optimal weights $w_{e,i}$.

Smaller field sizes have similar shape in the depth dependence of electron contamination dose, but the ratio of the electron contamination dose to the primary photon dose is smaller. The shape is nearly the same for all field sizes, since the spectrum of contaminant electrons does not vary significantly across the field (see e.g. Ding (2002)). To determine a proper field size dependence, the difference curve $\delta_{FS}(z)$ is calculated for smaller field sizes FS to determine a factor by which $\delta_{MaxFs}(z)$ should be scaled down to obtain $\delta_{FS}(z)$. This gives an optimal field size dependent scaling factor to which the calculations are fitted. The calculated scaling factor for arbitrary values of $\sigma_{e,i}$ $(i = 1, 2)$ and c is obtained by calculating the convolution of a square fluence of side length FS with both of the Gaussians and superimposing the results with weights c and $1 - c$. The value of the convolution on beam central axis relative to the value for the largest field size determines the calculated scaling factor. The parameters $\sigma_{e,i}(i = 1, 2)$ and c are then determined by minimizing the squared difference between the calculated and optimal scaling factors for all field sizes. The square fluence is an approximation of the primary fluence, which also includes the intensity profile $I(r)$, but this approximation has a negligible effect on the convolution value on the beam central axis.

2.4. Beam data measurements

In order to analyse the flexibility of the source model to characterize different treatment units and the performance of the optimization procedure, the model parameters were derived for different beam data sets representing linear accelerators from three major machine vendors: Varian Medical Systems (Palo Alto, CA, USA), Elekta (Stockholm, Sweden) and Siemens Medical Solutions (Malvern, PA, USA). The Varian accelerator differs from the other accelerators in that the open beam characteristics (field size, penumbra and output factors) are solely defined by the main X and Y collimators, and the MLC can be regarded as an add-on. All measurements for a Varian accelerator were performed on a Clinac 2100 C/D (6 MV and 15 MV). For both the Elekta and Siemens machines, the MLC is part of the main collimators. On the Siemens Primus accelerator, the lower jaw is entirely replaced by an MLC, whereas on the Elekta, the upper jaw is replaced partially by the MLC and partially by a thinner back-up jaw (Huq *et al* 2002). Hence, the MLC also defines the open field size and influences the penumbra for the Elekta and Siemens machines. For the evaluation purposes, the profile measurements were performed in the direction of the MLC leaf movement for an Elekta SL-18 (6 MV and 15 MV) and for a Siemens Primus (6 MV and 23 MV), since these are expected to be the most difficult to model. An additional data set on the Elekta SL-18 (6 MV) was obtained in the direction perpendicular to the leaf motion. Varian and Elekta beam data were measured in Helsinki University Central Hospital (Helsinki, Finland) and the Siemens beam data in Brigham and Women's hospital (Boston, MA, USA). All measurements were performed with an IC15 ionization chamber (Scanditronix Wellhöfer, Schwarzenbruck,

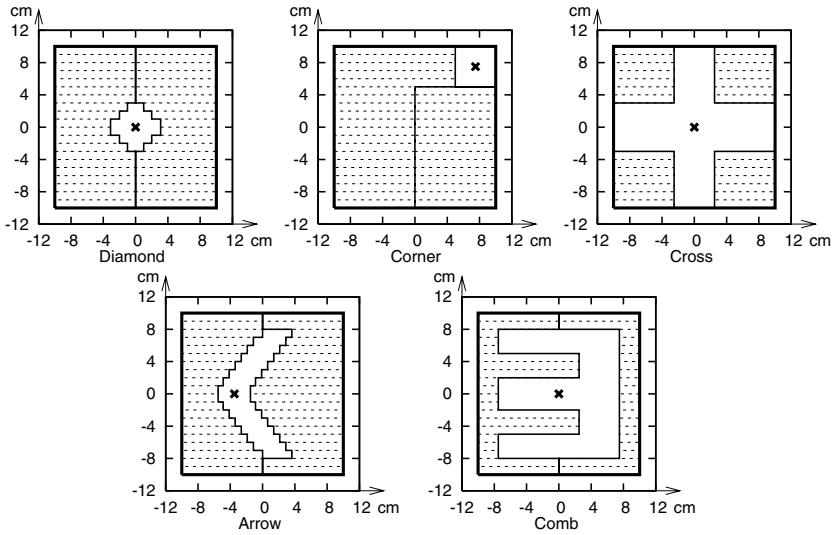

Figure 1. An illustration of the irregular MLC-shapes used for point dose measurements. The measurement point is marked with a cross 'x' in each MLC-collimated field.

Germany) having a volume of 130 mm^3 and with a Wellhöfer Blue Phantom with dimensions of $480 \times 480 \times 410\,mm^3$.

To verify that the source model and the optimized parameters are physical, comparisons between measurements and calculations were performed under conditions that were significantly different from the measurement conditions used in parameter derivation. These measurements were performed on a Varian Clinac 2100C/D accelerator for 6 MV and 15 MV photon beams. To study the effect of varying source-to-surface distance (SSD), central axis PDDs were measured for 50×50, 100×100, 200×200 and $300 \times 300\,mm^2$ fields at the SSDs of 810 mm and 1190 mm. The absolute dose at 50 mm depth was also measured for these fields. To study the accuracy of the backscatter modelling, PDDs (along axis going through the centre of the field at 50 mm depth) and point doses at 50 mm depth were measured for two asymmetric fields. The first field was a $50 \times 50\,mm^2$ field with centre point at (45, 75) mm, and the second field was a $400 \times 50\,mm^2$ field with centre point at (0, 125) mm. To study especially the modelling of the extra-focal radiation, point dose measurements were performed for five irregularly shaped MLC apertures at 50 mm depth at SSD 1000 mm (see figure 1). The Varian Millenium^{TM} 80 MLC was used in the measurements. The jaws were fixed to $200 \times 200\,mm^2$ for all of the MLC apertures. The same detector and water phantom were used as in the standard beam data measurements above.

3. Results and discussion

3.1. Convergence, robustness and accuracy of the optimization procedure

The convergence of the objective function in (13) during the first optimization phase for a Varian 2100C/D 15 MV beam is presented in figure 2. The objective function converges close to the final result within about 500 function evaluations, which corresponds to five iterations in the Powell's search algorithm. After that, the objective function value changes at

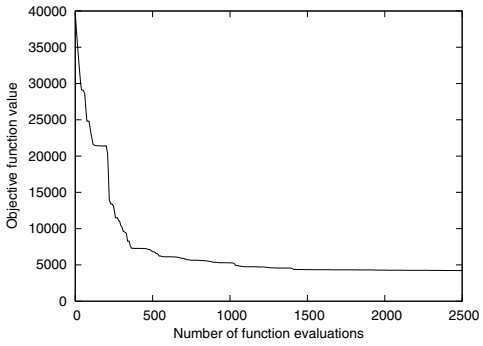

Figure 2. The objective function value as a function of the number of function evaluations during the first optimization phase for a Varian 2100C/D 15 MV beam.

a considerably slower rate. The processing time for the 500 function evaluations was 1 min on a 3.06 GHz Intel Xeon level computer with two processors and 2 GB of RAM. Time required for a complete parameter optimization varied from 30 to 60 min. The authors believe that the obtained calculation times are clinically acceptable, since the optimization process needs to be run only once during the beam configuration phase.

The robustness of the proposed procedure against different initial parameter values was analysed using two sets of extreme parameter values. The measured beam data were the same as in the previous example. In the first case, initial $\bar{E}(r)$ was equal to 6 MeV for all radial distances, $I(r)$ was set to increase linearly from 1.0 at the central axis to 1.15 at $r = 350$ mm and the following values were used for extra-focal source parameters: $w_{\mathrm{ef}} = 0.15$, $\bar{E}_{\mathrm{ef}} = 2.5$ MeV and $\sigma_{\mathrm{ef}} = 60$ mm. In the second case, $\bar{E}(r)$ was a constant 2 MeV, $I(r)$ was a constant 1.0 and the extra-focal source parameters were: $w_{\mathrm{ef}} = 0.01$, $\bar{E}_{\mathrm{ef}} = 0.7$ MeV and $\sigma_{\mathrm{ef}} = 15$ mm. When the optimization was performed using these two sets of initial parameter values, the resulting relative difference in the final objective function value was 0.4%. The following differences were obtained for the optimized parameter values: $\Delta\sigma_{\mathrm{ef}} = 0.22$ mm, $\Delta\bar{E}_{\mathrm{ef}} = 0.001$ MeV, $\Delta w_{\mathrm{ef}} = 8 \times 10^{-5}$, $\Delta\sigma_{\mathrm{e},1} = 0.42$ mm, $\Delta\sigma_{\mathrm{e},2} = 0.19$ mm, $\Delta c = 0.003$, $\max_r\{\Delta\bar{E}(r)\} = 0.28$ MeV and $\max_r\{\Delta I(r)\} = 0.007$ MeV. The observed differences in $c_{\mathrm{e}}(z)$ were negligible for the two cases. For this example case, the differences in the parameter values were very small with the exception of mean energy $\bar{E}(r)$ at radial distance $r = 250$ mm. This particular point in $\bar{E}(r)$ has negligible effect on the calculated dose and consequently on the objective function value, and can therefore vary somewhat between different initial values.

The effect of the approximate $M_{\mathrm{p.d.}}$ method on the final dose distribution was analysed by calculating the difference in dose distributions obtained from $M_{\mathrm{v.d.}}$ and $M_{\mathrm{p.d.}}$, $\Delta(\mathbf{x}) = \boldsymbol{D}_{\mathrm{v.d.}}(\boldsymbol{x}) - \boldsymbol{D}_{\mathrm{p.d.}}(\boldsymbol{x})$, before step (iv) ($\Delta_1$) and after step (v) ($\Delta_2$) of the procedure (see section 2.3). The possible difference between Δ_1 and Δ_2 is caused by different behaviours of the calculation methods when the model parameters are changed; if $\Delta_1 = \Delta_2$, the calculation methods behave identically and running steps (iv) and (v) again would produce no change in the optimized parameter set. The test data set was the same as in two previous examples and the first set of initial parameters from the previous example was used. The differences between Δ_1 and Δ_2 were mostly smaller than 0.1%, and larger discrepancies were detected only in the build-up region of the smallest field sizes (maximum difference 1% for 30×30 mm^2 field at the depth of 10 mm). The error in the final dose caused by the use of $M_{\mathrm{p.d.}}$ can be well

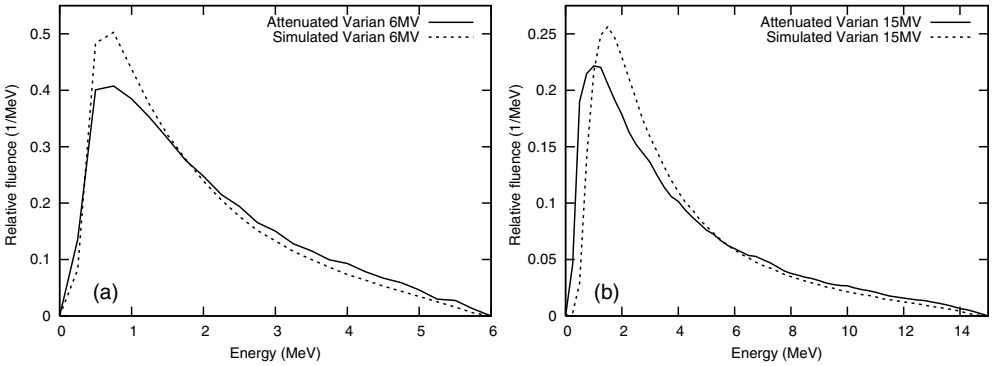

Figure 3. Comparison of photon beam spectra obtained from full Monte Carlo simulations (Sheikh-Bagheri and Rogers 2002a) of the accelerator head ('Simulated') and the attenuated spectra resulting from the proposed optimization process ('Attenuated') on beam central axis. The simulated spectra contain also extra-focal photons whereas the attenuated spectra contain only primary photons that have not interacted anywhere else than in the target. (a) Varian 6 MV beam, and (b) Varian 15 MV beam.

approximated with the difference between Δ_1 and Δ_2, which was mostly less than 0.1%. Even this difference can be easily compensated by running steps (iv) and (v) in a loop until the difference no longer changes. Due to the small magnitude of the difference, such an iteration was considered unnecessary.

3.2. Assessment of optimized model parameters

It has been shown previously that different photon spectra can result in similar PDDs in water over a range of field sizes (Charland *et al* 2004). Therefore, a spectrum that has been determined based on PDD measurements in water might not be physical. Inaccuracies in the spectrum could be detected as a mismatch between measurements and calculations in heterogeneous water–lung interfaces. In order to demonstrate that the photon spectra resulting from the optimization process are physical, MC simulated (Sheikh-Bagheri and Rogers 2002a) and attenuated spectra of the model were compared on the beam central axis. The comparison for 6 MV and 15 MV photon beams for the Varian accelerator is presented in figure 3. It should be noted that the reference spectra contain both primary and extra-focal photons whereas the attenuated spectra of the current model contain only primary photons.

In general, the shapes of the attenuated spectra are similar to the MC simulated spectra. Both simulated spectra contain a higher peak in the low-energy region than the attenuated spectra, which is likely to be caused by the missing extra-focal radiation in the attenuated spectra. Individual machine differences or different electron beam spot sizes in MC simulations can also explain some of the detected differences. The observed differences in the spectrum shapes are so small that they most likely do not affect calculated PDDs significantly even in water–lung interfaces. An explanation for this is that only the mass thickness of flattening filter (used to attenuate an initial spectrum) is deduced from the PDD measurements.

The optimized mean energy curves $\bar{E}(r)$ for Varian (6 MV, 15 MV), Elekta in the X-direction (6 MV, 15 MV), and Siemens (6 MV, 23 MV) are presented in figure 4(a). The mean radial energy curve for the beam data measured in the Y-direction of the Elekta machine is not presented, since it is very similar to the corresponding curve in the X-direction. The optimized mean energy on the beam central axis varies from 1.94 MeV (Varian 6 MV) to 4.8 MeV

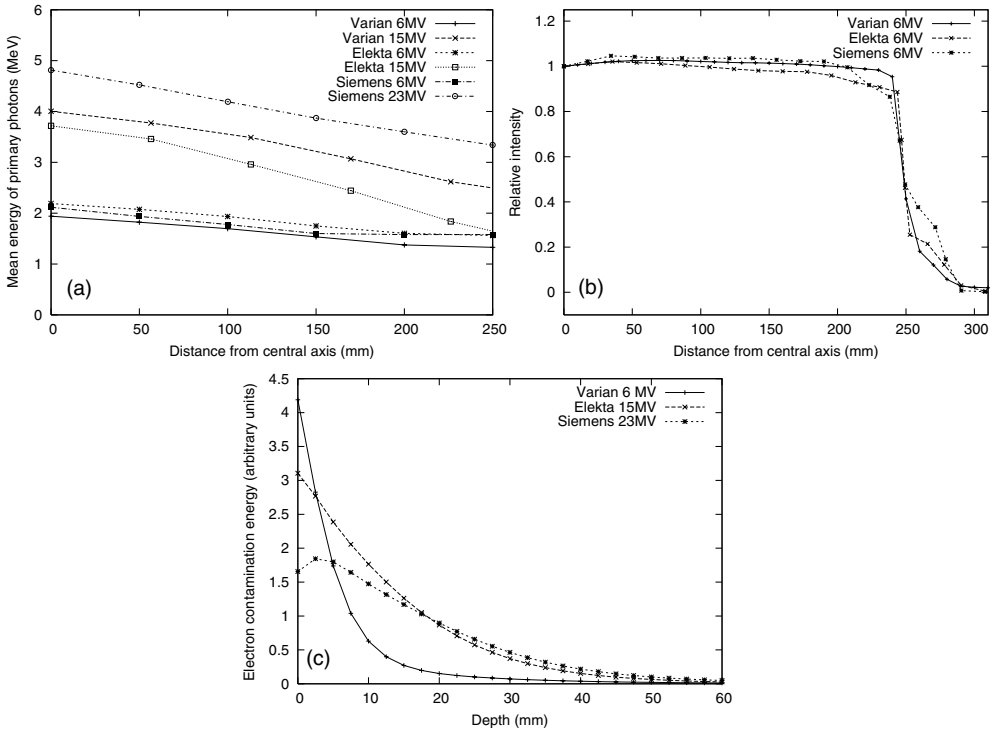

Figure 4. (a) Optimized mean radial energy curves $\bar{E}(r)$ for primary photons for six treatment beams (Varian 6 MV, Varian 15 MV, Elekta 6 MV, Elekta 15 MV, Siemens 6 MV and Siemens 23 MV), (b) optimized intensity profile curves $I(r)$ for Varian, Elekta, Siemens 6 MV beams, and (c) optimized electron contamination curves $c_e(z)$ for Varian 6 MV, Elekta 15 MV and Siemens 23 MV beams.

(Siemens 23 MV), being significantly lower than the nominal energy of the corresponding beam. The optimized mean energies are in good agreement with the MC simulated results reported by Sheikh-Bagheri and Rogers (2002a). For Varian and Siemens 6 MV beams, the optimized mean energy values are slightly (0.15 MeV) larger than reported. The agreement is better for the Elekta 6 MV and Varian 15 MV cases (no reference data available for Elekta 15 MV and Siemens 23 MV). The shape of the optimized intensity profile $I(r)$ varies somewhat between different accelerator vendors as can be seen in figure 4(b). Near the beam edge, $I(r)$ of the Siemens 6 MV beam decreases more slowly than the corresponding curve for Varian 6 MV and Elekta 6 MV beam. The differences in $I(r)$ between the accelerator vendors are likely caused by different flattening filter constructions. The optimized electron contamination curves $c_e(z)$ for Varian 6 MV, Elekta 15 MV and Siemens 23 MV beams are presented in figure 4(c). The integral of the electron contamination curve increases as the nominal energy increases (especially from 6 MV to 15 MV) indicating larger deposited contaminant electron dose. These curves are qualitatively similar to previously published MC simulated electron depth doses (Ding 2002).

The optimized extra-focal and electron contamination parameters for the six studied treatment beams are presented in table 2. The weight of the extra-focal source (w_{ef}) with respect to the primary source varies from 2.3% (Elekta 15 MV) to 4.2% (Siemens 6 MV). These values are lower than reported in previous studies, e.g. 10%, ..., 20% in Liu *et al*

Table 2. The optimized extra-focal source weight w_{ef} (%), size σ_{ef} (mm), energy $\bar{E}_{ef}$ (MeV) and electron contamination parameters c (%), $\sigma_{e,1}$ (mm), $\sigma_{e,2}$ (mm) for the different treatment beams studied. For the Elekta SL-18 treatment unit, measurements have been conducted in two orthogonal directions (X and Y) for the 6 MV nominal energy.

Machine	w_{ef}	σ_{ef}	$\bar{E}_{ef}$	c	$\sigma_{e,1}$	$\sigma_{e,2}$
Varian 2100C/D 6 MV	3.8	30.5	0.68	31	7.4	77.1
Varian 2100C/D 15 MV	2.5	31.0	0.64	46	13.7	60.2
Elekta SL-18 6 MV (X)	3.3	35.1	0.73	22	13.2	77.6
Elekta SL-18 15 MV (X)	2.3	33.2	0.68	54	12.8	74.2
Elekta SL-18 6 MV (Y)	2.7	35.7	0.55	27	6.3	77.8
Siemens Primus 6 MV	4.2	27.3	0.73	26	18.5	121.9
Siemens Primus 23 MV	3.4	24.8	0.71	22	24.0	83.0

(1997b). However, in the proposed model w_{ef} is defined as the ratio in energy fluences, whereas in Liu *et al* (1997b) it has been defined as a ratio in particle fluences. Since the energy of the extra-focal photons is considerably lower than the energy of primary photons, these two figures are not in contradiction. One might also expect to see an increase in the extra-focal source weight as the nominal energy increases, which was not observed in the present work. However, since the mean energy of primary photons increases more than the mean energy of the extra-focal photons as the nominal energy increases (Sheikh-Bagheri and Rogers 2002a), the ratio in energy fluences may remain approximately constant.

The size of the extra-focal source (σ_{ef}) in table 2 varies from 27 mm to 36 mm. These are close to previously reported values for the extra-focal source size, where the radius of a circular disc has been reported to vary from 10 mm to 17.5 mm (Liu *et al* 1997b). The mean energy of the extra-focal photons ($\bar{E}_{ef}$) varies from 0.55 MeV to 0.73 MeV in table 2. These are lower values than reported in previous studies (Sheikh-Bagheri and Rogers 2002a) and do not increase as a function of nominal energy as would be expected. One possible explanation is that the empirical extra-focal source spectrum used in the source model contains unrealistically high energy components. Lack of increase in the extra-focal source energy as a function of nominal energy might be caused by the fact that several parameters in the model have an influence on the dose in the profile tail region. Therefore, the effect of the extra-focal source energy cannot be necessarily distinguished from the effect of the other parameters. However, as reported in the following sections, measured and calculated doses in the profile tail region are in good agreement for all machine vendors and energies regardless of the slightly unphysical energy values.

3.3. Comparisons of dose calculations and measurements used in the optimization

In deriving the model parameters for the different treatment units described in section 2.4, the distance parameters, flattening filter materials and initial photon spectra for Varian treatment units were also used for other accelerator vendors due to lack of information about these parameters for other vendors. To analyse the success of the optimization, a gamma error distance (γ) was computed separately between each measurement point and the corresponding dose curve calculated with $M_{v.d.}$. A grid size of 2.5 mm was used in volumetric dose calculation, and the dose values were linearly interpolated between grid points in the computation of the gamma errors. Calculations were compared to the measurements that were adjusted as explained in section 2.3.1. The profiles were scaled with the value taken from the corresponding PDD at the profile measurement depth. The maximum of the measured PDD

Table 3. Average (Ave) and maximum (Max) gamma error values (1%, 1 mm), and the percentage of points (P) passing the $\gamma < 1$ criterion for field sizes 40×40, 100×100, 200×200 and $400 \times 400\,\text{mm}^2$ (FS40, FS100, FS200 and FS400) for the six treatment beams analysed. The average value is calculated over depth dose curves, lateral profiles and possible diagonal profiles for each field size. For the Elekta SL-18 treatment unit, measurements have been conducted in two orthogonal directions (X and Y) for the 6 MV nominal energy.

	FS40			FS100			FS200			FS400		
	Ave	Max	P (%)	Ave	Max	P (%)	Ave	Max	P (%)	Ave	Max	P (%)
Varian 6 MV	0.3	1.1	99.5	0.3	1.6	96.4	0.2	1.7	96.2	0.3	2.5	96.2
Varian 15 MV	0.3	0.9	100.0	0.3	1.4	97.6	0.3	1.3	97.4	0.3	1.9	95.7
Elekta 6 MV (X)	0.4	2.4	90.1	0.3	2.9	92.2	0.3	2.8	93.8	0.3	2.1	95.1
Elekta 15 MV (X)	0.6	2.0	89.6	0.5	2.5	90.8	0.4	2.5	89.7	0.5	3.6	84.8
Elekta 6 MV (Y)	0.2	1.2	98.1	0.2	1.2	99.5	0.2	1.4	96.7	0.3	2.7	95.1
Siemens 6 MV	0.6	2.1	85.1	0.5	3.1	88.5	0.5	2.3	88.3	0.4	2.3	89.1
Siemens 23 MV	0.7	2.1	82.6	0.5	2.3	89.2	0.4	1.8	90.9	0.5	2.7	91.1

was normalized to 100%, and the calculated PDD was normalized to the measured PDD at 50 mm depth.

To provide a very general overview, the average and maximum γ error (1%, 1 mm) as well as the percentage of measurement points passing the $\gamma < 1$ criterion for a representative set of field sizes are shown in table 3 for each of the seven studied treatment beams. The error values for a certain field size have been calculated over the measurement points located in the PDD, lateral profiles and possible diagonal profiles for the corresponding field size. The average γ is in the order of 0.5 for all field sizes and treatment units studied. The maximum γ varies from 0.9 (Varian 15 MV, FS40) to 3.6 (Elekta 15 MV, FS400). The percentage of measurement points passing the $\gamma < 1$ criterion varies from 82.6% to 100%, being larger for the Varian beam data (95%, ..., 100%) than for the Elekta and Siemens beam data (83%, ..., 99.5%). For the Elekta machine, the gamma errors are smaller in the Y-direction than in the X-direction. The results for the Y-direction for the Elekta machine are comparable to the results for the Varian machine.

Figures 5–7 present a visual overview of the obtained results, showing measured and calculated PDDs and profiles for Varian 6 MV, Elekta 15 MV (X-direction) and Siemens 23 MV. All data have been normalized to 100% at 50 mm depth. Regarding the PDDs, there is good visual agreement between measurements and calculations for each case. The deviations in the PDDs are all smaller than 1%, 1 mm except for depths smaller than 15 mm. Regarding profiles, best results are obtained for the Varian treatment unit (figure 5). For Varian, the largest discrepancies occur in the field penumbra but do not exceed 2%, 2 mm. For the Elekta 15 MV and Siemens 23 MV beams in figures 6 and 7, the results are comparable within the open field, but the deviations in the penumbra exceed 2%, 2 mm. The volume averaging effect of the ionization chamber has been identified as a partial cause for the observed deviations in the penumbra region for each studied beam data set. The broadening caused by the ionization chamber can be up to 1 mm on both sides of the 50% isodose (Garcia-Vicente *et al* 1998). There are also deviations around 2%, 2 mm visible in the topmost profile of the $400 \times 400\,\text{mm}^2$ field in figures 6 and 7. These deviations are likely caused by the relatively simple model used for electron contamination, where only the PDDs have an effect on the electron contamination parameters.

For the X-direction of the Elekta machine (figure 6), there are deviations between 2%, 2 mm and 3%, 3 mm in the penumbra of each field size. In the dose calculations, the 50%

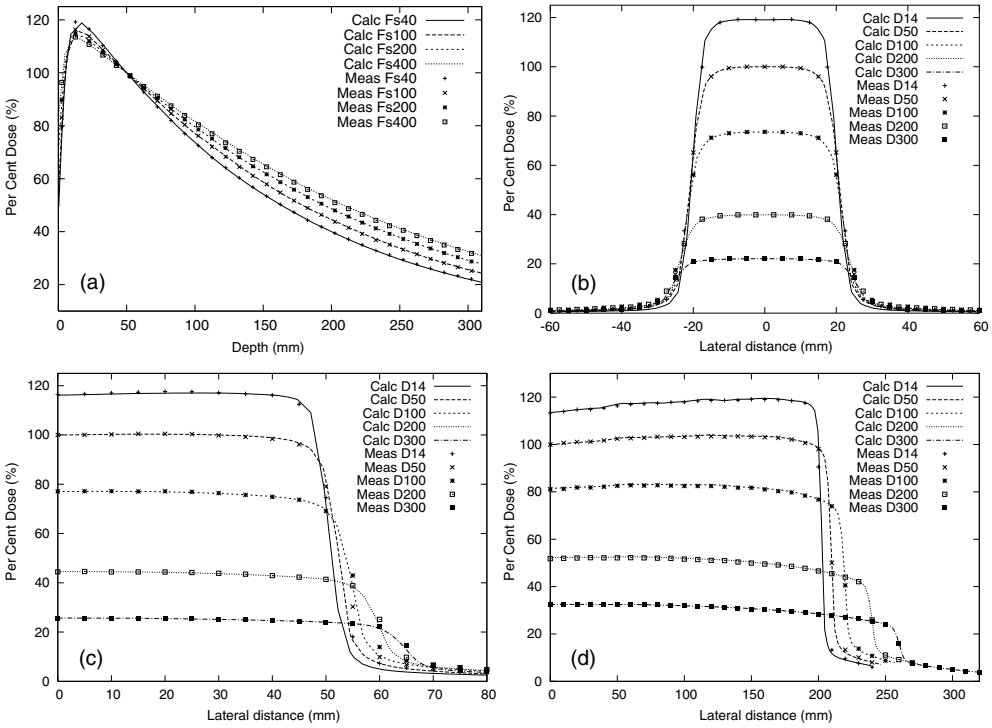

Figure 5. Comparison of measured (Meas) and calculated (Calc) central axis depth dose curves and lateral dose profiles for a Varian 2100C/D 6 MV accelerator. (a) Central axis depth dose curves, (b) lateral profiles for a $40 \times 40\,\mathrm{mm}^2$ field, (c) $100 \times 100\,\mathrm{mm}^2$ field and (d) $400 \times 400\,\mathrm{mm}^2$ field. The field size in millimetres is indicated in the figure label after the symbol 'Fs' and the profile measurement depth after the symbol 'D'. Doses are normalized to 100% at a depth of 50 mm along the beam central axis for each field.

isodose is located at the nominal field border, whereas the measurement shows a slightly ($\sim$1 mm) displaced field border, resulting in an effective field width of $\sim$2 mm smaller than the nominal field width. This discrepancy is related to the mechanical construction of the MLC/back-up jaw combination. The displacement of the 50% isodose caused by the rounded leaf tips of the MLC is taken into account during the MLC calibration. However, when the back-up jaws are calibrated too close to the outer point of the leaf tips—as is often the case—they cause a shift in the penumbra, reducing the effective field size of the open fields by typically $\sim$1 mm on both sides. This is not accounted for in the current multiple-source model. The measured penumbra for the Elekta accelerator is also somewhat broader in the *X*-direction than in the *Y*-direction (see figure 8). Possible causes for this phenomenon are transmission through the rounded MLC leaf tips and/or the finite focal spot size for the brehmsstrahlung target, which are not currently taken into account in the source model. The finite focal spot may have different effects in *X*- and *Y*-directions, since the collimators are located at different distances from the target. The focal spot may also be asymmetric in *X*- and *Y*-directions as suggested by earlier studies (Jaffray *et al* 1993). To improve correspondence between measurements and calculations, preferably, one should calibrate the back-up jaws to obtain a 50% isodose value at the nominal field edge. Alternatively, a displacement parameter could be introduced into the model to account for the 50% isodose shift. To account for

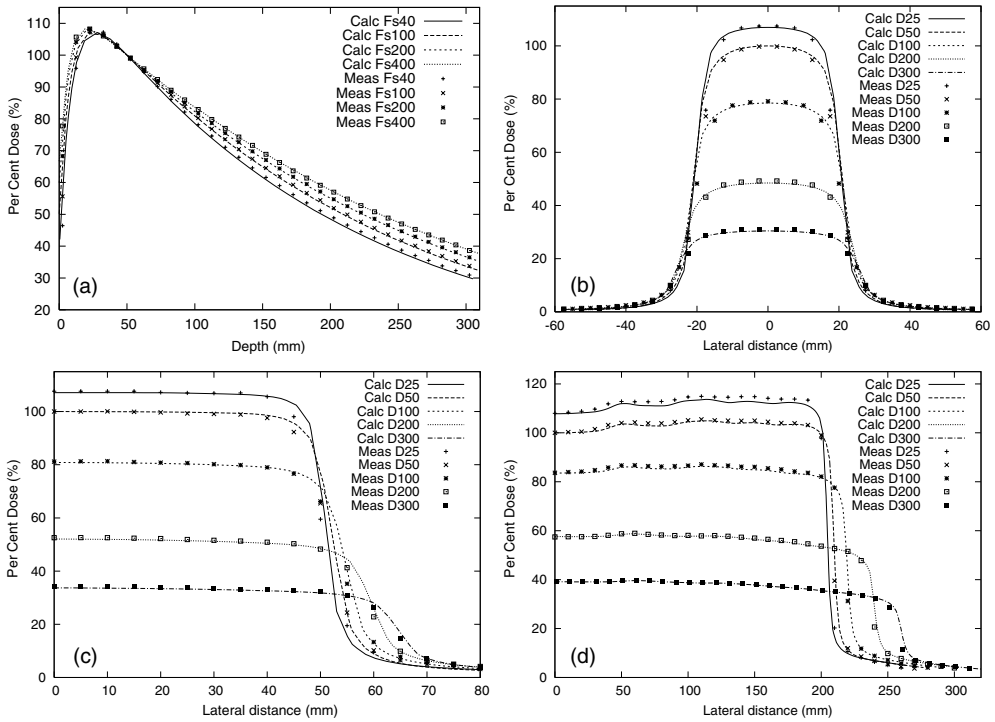

Figure 6. Comparison of measured (Meas) and calculated (Calc) central axis depth dose curves and lateral dose profiles in the direction of MLC movement (X) for an Elekta SL-18 15 MV accelerator. (a) Central axis depth dose curves, (b) lateral profiles for a $40 \times 40\,\mathrm{mm}^2$ field, (c) $100 \times 100\,\mathrm{mm}^2$ field and (d) $400 \times 400\,\mathrm{mm}^2$ field. The field size in millimetres is indicated in the figure label after the symbol 'Fs' and the profile measurement depth after the symbol 'D'. Doses are normalized to 100% at a depth of 50 mm along the beam central axis for each field.

the additional broadening in the penumbra for the X-direction, a separate spot size parameter could be introduced in the primary photon source model for X- and Y-directions. Transmission through the rounded MLC leaf tips could also be included in the model for static cases by modifying the modulating function $F_{\mathrm{MLC}}(x, y)$.

For the Siemens treatment unit, the deviations in the penumbra are similar to the deviations observed for the Elekta treatment unit—there is a positional shift of $\sim$1 mm between the calculated and measured 50% isodose value. The origin of the discrepancy is again the mechanical calibration, in this case of the MLC itself. Although the MLC has straight edges that should be focused for all field sizes, it is a known problem for the Siemens Primus that the border of the light field does not coincide with the 50% isodose of the irradiated field in the direction of the MLC. When the jaw/MLC calibration is performed by means of the light field, the effective field size is again smaller than the nominal field size. The shift is again of the order of $\sim$1 mm, but varies slightly as a function of off-axis position of the MLC. In the direction perpendicular to the MLC, no such deviation exists. When the measured penumbra data are shifted to make the 50% dose value coincide with the nominal field edge (figure 9), correspondence is improved, and the maximum gamma errors are reduced from 3.1 to 2.1 for 6 MV and from 2.3 to 2.0 for 23 MV. Although improved mechanical calibration would again be the preferred solution, an alternative solution would consist of introducing a displacement

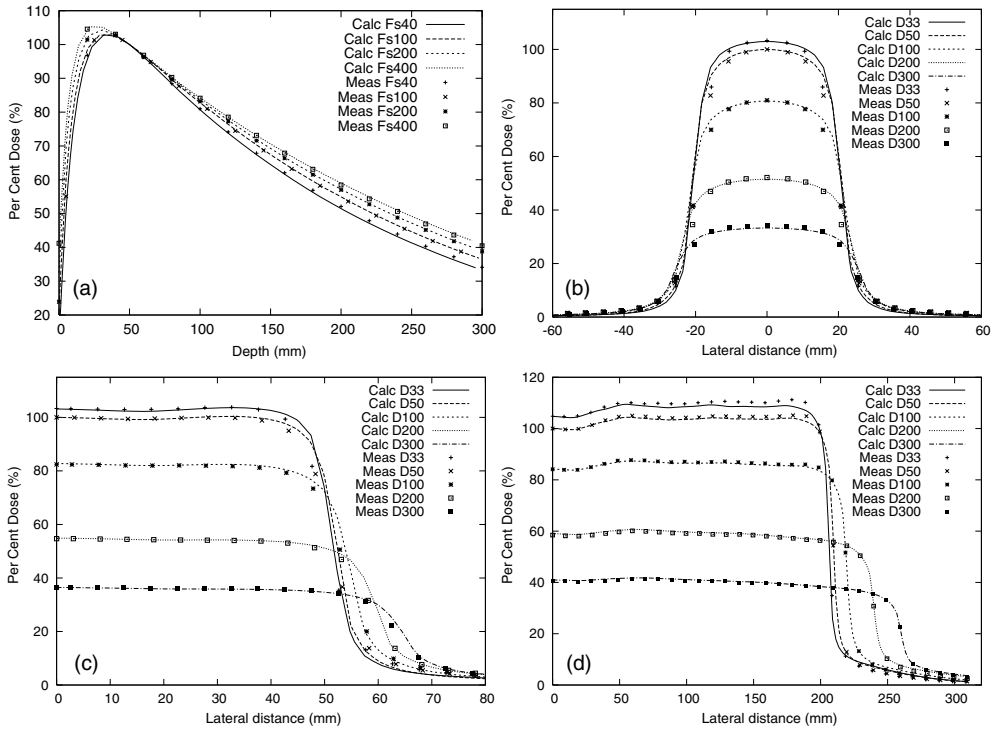

Figure 7. Comparison of measured (Meas) and calculated (Calc) central axis depth dose curves and lateral dose profiles in the direction of MLC movement (X) for a Siemens Primus 23 MV accelerator. (a) Central axis depth dose curves, (b) lateral profiles for a $40 \times 40\,\mathrm{mm}^2$ field, (c) $100 \times 100\,\mathrm{mm}^2$ field and (d) $400 \times 400\,\mathrm{mm}^2$ field. The field size in millimetres is indicated in the figure label after the symbol 'Fs' and the profile measurement depth after the symbol 'D'. Doses are normalized to 100% at a depth of 50 mm along the beam central axis for each field.

parameter to the model. The fact that the penumbra in the calculated profile is still too sharp after the displacement of the measured profile could be due to larger focal spot in the Siemens treatment unit compared to the Varian treatment unit.

In general, the authors believe that the obtained accuracy is sufficient for treatment planning calculations for each studied accelerator type. A discrepancy of 1%, 1 mm in the penumbra can be attributed to the finite dimensions of the used ionization chamber for all beam data sets. If the mechanical calibration issues on the Siemens and Elekta treatment units are resolved, an overall 2%, 2 mm accuracy can be obtained with the current model.

3.4. Comparison of calculations and measurements at different SSDs

Measured and calculated PDDs at absolute dose scale for two different SSDs (810 mm and 1190 mm) and for two beam energies (6 MV and 15 MV) are illustrated in figure 10. The average and maximum γ (1%, 1 mm) for each field are presented in table 4. In the γ-calculation, the measured doses were normalized to 100% at $d_{\max}$ for each field, and the calculations were normalized using the same scaling factor. The obtained average γ is smaller than 1.1 for all of the studied cases. The maximum γ varies from 0.8 to 2.8, being largest for SSD 810 mm for the 15 MV beam. The agreement between measurements and calculations is

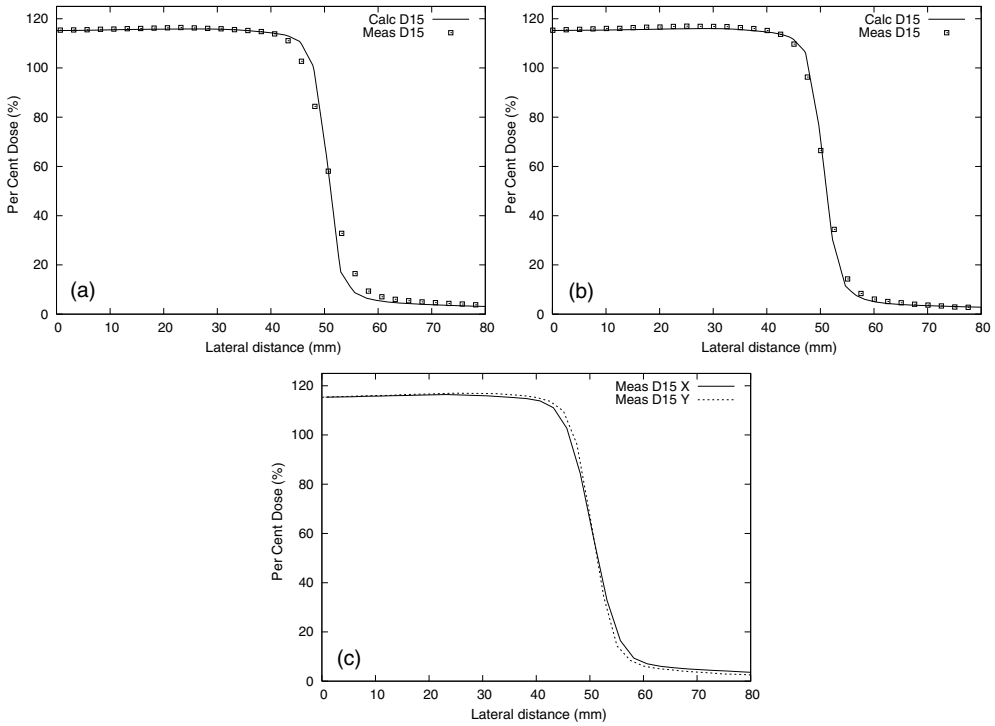

Figure 8. The effect of the measurement direction on the penumbra of a $100 \times 100\,\mathrm{mm}^2$ field at $d_{\max}$ for an Elekta SL-18 treatment unit with 6 MV nominal energy. (a) Comparison of dose calculations and measurements in the *X*-direction (along the axis of MLC movement), (b) comparison of dose calculations and measurements in the *Y*-direction (along the axis perpendicular to MLC movement) and (c) inter-comparison of measurements in *X*- and *Y*-directions. Both measured profiles have been shifted so that the 50% isodose coincides with the expected value defined by the nominal field size.

Table 4. Average (Ave) and maximum (Max) gamma error values (1%, 1 mm) for field sizes 50×50, 100×100, 200×200 and $300 \times 300\,\mathrm{mm}^2$ (FS50, FS100, FS200 and FS300) at SSDs 810 mm and 1190 mm for Varian 2100C/D 6 MV and 15 MV beams. Depths smaller than 5 mm have been ignored in the computation of the gamma errors. The average value is calculated over the depth dose curves for each field size.

Field size	Energy	SSD 810 mm		SSD 1190 mm	
(mm^2)	(MV)	Ave	Max	Ave	Max
FS50	6	0.2	1.5	0.3	0.9
FS100	6	0.4	1.2	0.2	1.0
FS200	6	0.5	1.8	0.2	1.1
FS300	6	0.4	1.6	0.2	1.4
FS50	15	0.7	2.8	0.4	1.0
FS100	15	0.7	2.8	0.3	1.1
FS200	15	1.1	1.5	0.3	0.9
FS300	15	0.9	1.7	0.3	0.8

better with SSD 1190 mm than with SSD 810 mm. These results are only slightly inferior to the results obtained for the square fields that were used during the optimization process. This,

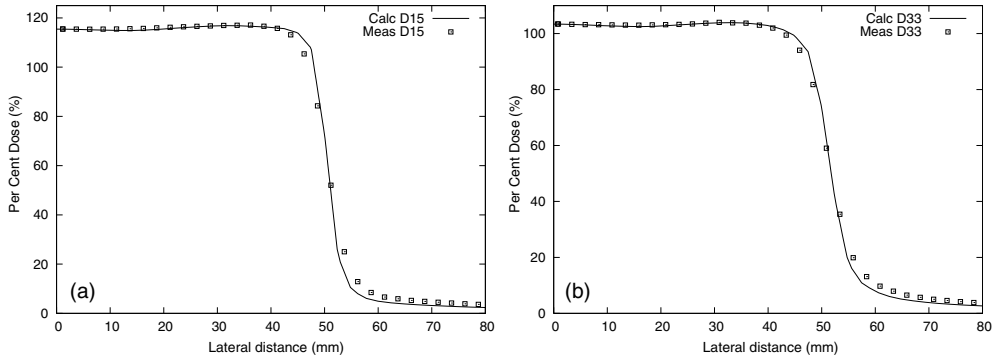

Figure 9. Comparison of measured and calculated profiles for a $100 \times 100\,\mathrm{mm}^2$ field at $d_{\max}$ for a Siemens Primus treatment unit. (a) Comparison of dose calculations and measurements for 6 MV, (b) comparison of dose calculations and measurements for 23 MV. Both measured profiles have been shifted so that the 50% isodose coincides with the expected value defined by the nominal field size.

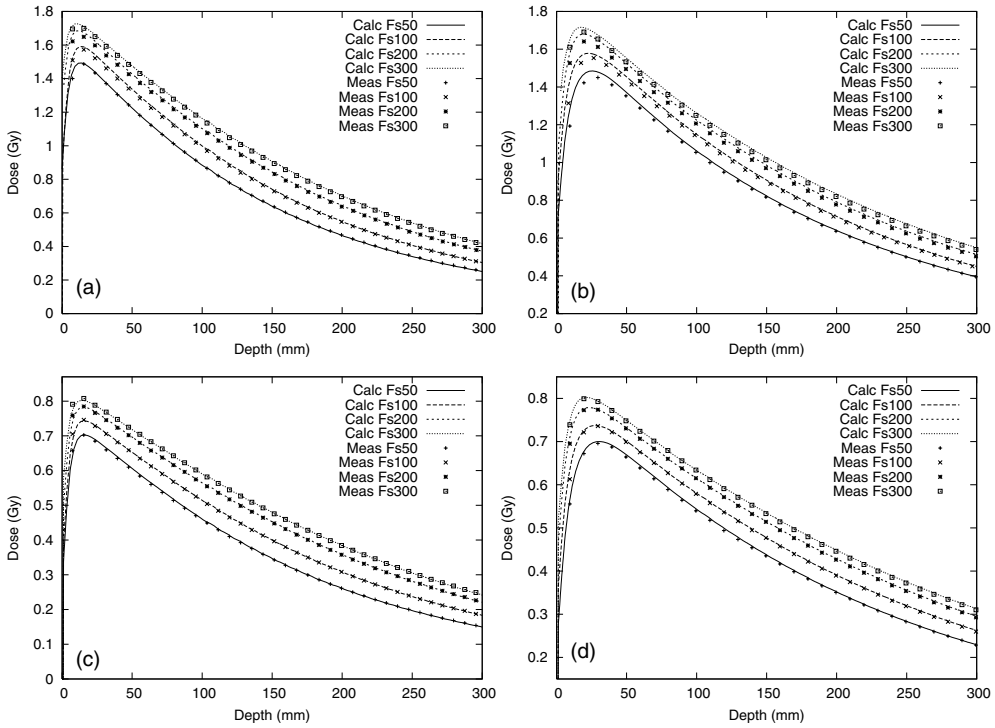

Figure 10. Measured (Meas) and calculated (Calc) central axis depth dose curves for field sizes 50×50, 100×100, 200×200 and $300 \times 300\,\mathrm{mm}^2$ for a Varian 2100C/D accelerator with (a) 6 MV photons at SSD 810 mm, (b) 15 MV photons at SSD 810 mm, (c) 6 MV photons at SSD 1190 mm and (d) 15 MV photons at SSD 1190 mm. The field size in millimetres is indicated in the figure label after the symbol 'Fs'. All the doses are in absolute scale (Gy).

together with the results presented in sections 3.5 and 3.6 indicates that the source model with the optimized parameters is physical.

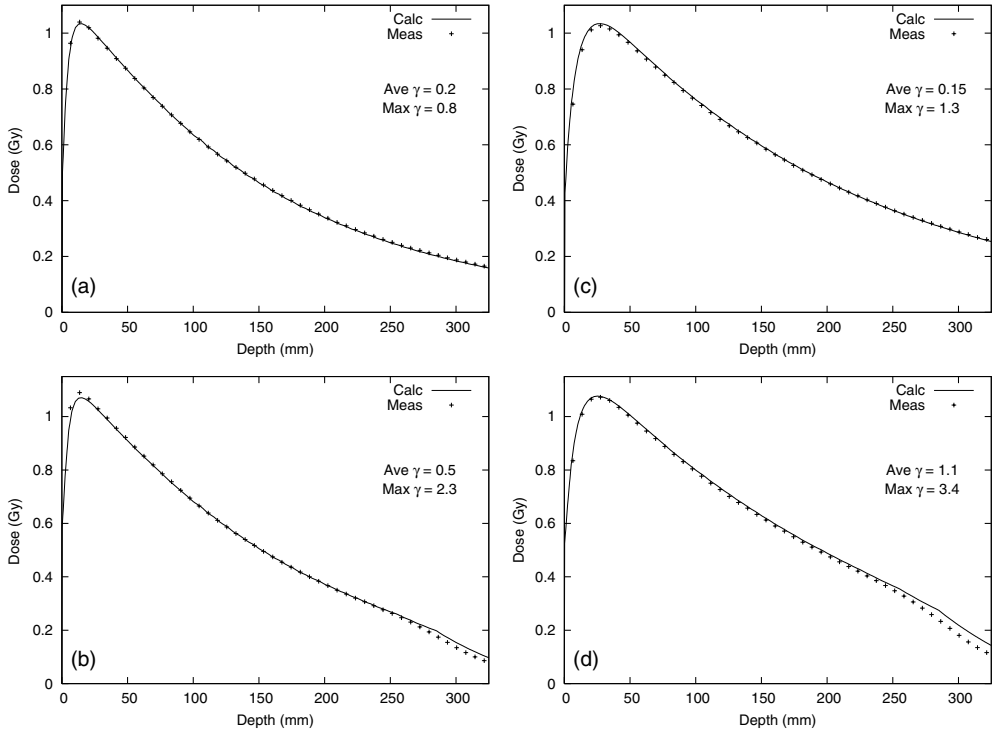

Figure 11. Measured (Meas) and calculated (Calc) depth dose curves for two asymmetric fields for a Varian 2100C/D accelerator. (a) 6 MV photons with $50 \times 50\,\mathrm{mm}^2$ field, (b) 15 MV photons with $50 \times 50\,\mathrm{mm}^2$, (c) 6 MV photons with $400 \times 50\,\mathrm{mm}^2$ field and (d) 15 MV photons with $400 \times 50\,\mathrm{mm}^2$ field. All the doses are in absolute scale (Gy).

3.5. Comparison of calculations and measurements for asymmetric fields

Measured and calculated PDDs at absolute dose scale for the two asymmetric fields defined in section 2.4 and for two beam energies (6 MV and 15 MV) are shown in figure 11. The maximum and average γ (1%, 1 mm) is indicated in each subfigure for the corresponding case. In the computation of γ, the doses were normalized in the same way as reported in section 3.4. The average γ is smaller than 1.1 for all of the cases. The largest deviation is seen for the $400 \times 50\,\mathrm{mm}^2$ 15 MV field, where the maximum gamma error is 3.4. There is an abrupt change in the dose at the depth of around 270 mm for the $400 \times 50\,\mathrm{mm}^2$ field, and larger discrepancies are observed below that point. At this point, the line along which the measurement probe moves enters into the field penumbra region, where the gradient of the dose distribution is large. These results indicate that the model for the collimator backscatter used is accurate also for asymmetric cases for the Varian accelerator.

3.6. Comparison of calculations and measurements for irregularly shaped MLC apertures

The measured and calculated point doses at 50 mm depth for the five irregular MLC apertures of figure 1 are presented in table 5. There is a very good agreement between measurements and calculations, since all calculations are within 1.0% of the measured values. Even though the scatter from the MLC leaves is not modelled in $M_{\mathrm{v.d.}}$, this approximation does not deteriorate the calculation accuracy for the studied static MLC fields. The good results for the irregular

Table 5. Measured (Meas) and calculated (Calc) point doses (Gy) at 50 mm depth at SSD 1000 mm corresponding to 100 monitor units for five irregularly shaped MLC apertures. The jaws have been fixed to 200 × 200 mm^2 position for all MLC apertures.

	6 MV			15 MV		
Field	Meas (Gy)	Calc (Gy)	Diff (%)	Meas (Gy)	Calc (Gy)	Diff (%)
Centre	0.867	0.869	0.2	0.951	0.958	0.7
Corner	0.895	0.897	0.2	0.994	0.990	−0.4
Cross	0.933	0.940	0.7	0.993	1.002	0.9
Arrow	0.893	0.895	0.3	0.987	0.987	0.0
Comb	0.905	0.914	1.0	0.975	0.978	0.3

MLC fields indicate that the extra-focal source model is capable of describing complicated field shapes created with the MLC. The purpose of the MLC tests in this work was to check the absolute dose calculation accuracy in the centre of the field opening to validate whether the used model parameters are physical. More detailed tests on the accuracy and limitations of the MLC modelling (static and dynamic fields) in the AAA algorithm were reported by Van Esch *et al* (2006).

4. Conclusions

This work demonstrates that it is possible to derive physical parameter values for a multiple-source model from simple beam data measurements using an automatic optimization-based process.

For a Varian accelerator, measurements and superposition/convolution dose calculations utilizing the optimized parameter values were in excellent agreement (mostly within 2%, 2 mm) in a wide range of conditions. Only a few parameters are required from the technical information about the accelerator. Therefore, the dose calculation algorithm utilizing the source model can be easily commissioned for clinical use in a hospital. In the future, the optimization procedure could be extended to take into account the output factor measurements in the derivation of e.g. extra-focal source model parameters. This would require a parameterized model of backscattered radiation into the monitor chamber. The profile measurements could be taken into account in the derivation of the electron contamination parameters to possibly obtain a better fit for the profiles in some cases. However, the presented model still results in acceptable accuracy in the build-up region. For the extra-focal photon source, a Monte Carlo simulated spectrum could be used to obtain more physical mean energy values for the extra-focal radiation.

For other machine vendors than Varian, the real geometry information and target materials should be used. However, since the presented multiple-source model contains several degrees of freedom, it was able to adjust well to measurements from Elekta and Siemens machines even though the Varian technical data were used. Discrepancies between calculated and measured open field profiles were primarily observed in the direction of the MLC movement, and were at least partially caused by a displacement of the effective field edge in the measured data related to the mechanical inaccuracies in the calibration of the collimators. Although this is an existing problem not accounted for in most of the currently available commercial treatment planning systems, one could take it into account with a displacement parameter in the dose calculations, if more accurate mechanical calibration is not possible. The source model could

be further refined by introducing an effective spot size parameter for the primary photon source to better model the shape of the penumbra for some cases. One should be careful, however, not to model the volume averaging effect of the ionization chamber with this parameter. For the Elekta treatment unit, the source model could be further improved by taking the rounded leaf ends of the MLC into account.

Acknowledgments

This work has been funded by Varian Medical Systems, Inc. The authors want to thank Dr Joseph H Killoran from Longwood Radiation Oncology Center for providing the beam data for the Siemens Primus accelerator (6 MV and 23 MV energies), Phil. Lic. Jukka Pyykkönen from Helsinki University Central Hospital for providing the beam data for the Varian 2100C/D and Elekta SL-18 accelerators (6 MV and 15 MV energies), as well as measurements for the different SSDs, asymmetric fields and irregularly shaped MLC apertures. The authors also want to thank Ann Van Esch, Dominique Huyskens, Katja Pesola and Tuomas Torsti for fruitful discussions.

References

Ahnesjö A 1989 Collapsed cone convolution of radiant energy for photon dose calculation in heterogeneous media *Med. Phys.* **16** 577–92

Ahnesjö A, Weber L, Murman A, Saxner M, Thorslund I and Traneus E 2005 Beam modeling and verification of a photon beam multisource model *Med. Phys.* **32** 1722–37

Boyer A L and Mok E C 1986 Calculation of photon dose distributions in an inhomogeneous medium using convolutions *Med. Phys.* **13** 503–9

Charland P M, Chetty I J, Paniak L D, Bednarz B P and Fraass B A 2004 Enhanced spectral discrimination through the exploitation of interface effects in photon dose data *Med. Phys.* **31** 264–76

Chetty I, DeMarco J J and Solberg T D 2000 A virtual source model for Monte Carlo modeling of arbitrary intensity distributions *Med. Phys.* **27** 166–72

Ding G X 2002 Energy spectra, angular spread, fluence profiles and dose distributions of 6 and 18 MV photon beams: results of Monte Carlo simulations for a Varian 2100EX accelerator *Phys. Med. Biol.* **47** 1025–46

Fippel M, Haryanto F, Dohm O and Nusslin F 2003 A virtual photon energy fluence model for Monte Carlo dose calculation *Med. Phys.* **30** 301–11

Fix M K, Keall P J, Dawson K and Siebers J V 2004 Monte Carlo source model for photon beam radiotherapy: photon source characteristics *Med. Phys.* **31** 3106–21

Fogliata A, Nicolini G, Vanetti E, Clivio A and Cozzi L 2006 Dosimetric validation of the anisotropic analytical algorithm for photon dose calculation: fundamental characterization in water *Phys. Med. Biol.* **51** 1421–38

Garcia-Vicente F, Delgado J M and Peraza J 1998 Experimental Determination of the convolution kernel for the study of the spatial response of a detector *Med. Phys.* **25** 202–7

Hubbell J H and Seltzer S M 2004 *Tables of X-ray Mass Attenuation Coefficients and Mass Energy-Absorption Coefficients (version 1.4)* (Gaithersburg, MD: National Institute of Standards and Technology)

Huq M S, Das I J, Steinberg T and Galvin J M 2002 A dosimetric comparison of various multileaf collimators *Phys. Med. Biol.* **47** N159–70

Jaffray D A, Battista J J, Fenster A and Munro B 1993 X-ray sources of medical linear accelerators: focal and extra-focal radiation *Med. Phys.* **20** 1417–27

Jiang S B, Boyer A L and Ma C M 2001 Modeling the extrafocal radiation and monitor chamber backscatter for photon beam dose calculation *Med. Phys.* **28** 55–66

Kawrakow I 2000 Accurate condensed history Monte Carlo simulation of electron transport I: EGSnrc, the new EGS4 version *Med. Phys.* **27** 485–98

Kawrakow I, Fippel M and Friedrich K 1996 3D electron dose calculation using a voxel based Monte Carlo algorithm (VMC) *Med. Phys.* **23** 445–57

Liu H H, Mackie T R and McCullough E C 1997a Calculating output factors for photon beam radiotherapy using a convolution/superposition method based on a dual source photon beam model *Med. Phys.* **24** 1975–85

Liu H H, Mackie T R and McCullough E C 1997b A dual source photon beam model used in convolution/superposition dose calculations for clinical megavoltage x-ray beams *Med. Phys.* **24** 1960–71

Liu H H, Mackie T R and McCullough E C 2000 Modeling photon output caused by backscattered radiation into the monitor chamber from collimator jaws using a Monte Carlo technique *Med. Phys.* **27** 737–44

Low D A, Harms W B, Mutic S and Purdy J A 1998 A technique for the quantitative evaluation of dose distribution *Med. Phys.* **25** 656–61

Mackie T R, Scrimger J W and Battista J J 1985 A convolution method of calculating dose for 15-MV x rays *Med. Phys.* **12** 188–96

Mohan R, Chui C and Lidofsky L 1986 Differential pencil beam dose computation model for photons *Med. Phys.* **13** 64–73

Naqvi S A, D'Sourza W D, Earl M A, Ye S-J, Shih R and Li X A 2005 Using a photon phase-space source for convolution/superposition dose calculations in radiation therapy *Phys. Med. Biol.* **50** 4111–24

Neuenschwander H, Mackie T R and Reckwerdt P J 1995 MMC-a high-performance Monte Carlo code for electron beam treatment planning *Phys. Med. Biol.* **40** 543–74

Powell M J D 1965 An efficient method for finding the minimum of a function of several variables without calculating derivatives *Comput. J.* **7** 155–62

Press W H, Teukolsky S A, Vetterling W T and Flannery B P 1999 *Numerical Recipes in C: The Art of Scientific Computing* 2nd edn (Cambridge: Cambridge University Press) p 397

Rogers D W, Faddegon B A, Ding G X, Ma C M, We J and Mackie T R 1995 BEAM: A Monte Carlo code to simulate radiotherapy treatment units *Med. Phys.* **22** 503–24

Schach von Wittenau A E, Cox L J, Bergstrom P M Jr, Chandler W P, Hartmann Siantar C L and Mohan R 1999 Correlated histogram representation of Monte Carlo derived medical accelerator photon-output phase space *Med. Phys.* **26** 1196–211

Sheikh-Bagheri D and Rogers D W O 2002a Monte Carlo calculation of nine megavoltage photon beam spectra using the BEAM code *Med. Phys.* **29** 391–402

Sheikh-Bagheri D and Rogers D W O 2002b Sensitivity of megavoltage photon beam Monte Carlo simulations to electron beam and other parameters *Med. Phys.* **29** 379–90

Ulmer W and Harder D 1995 A triple Gaussian pencil beam model for photon beam treatment planning *Z. Med. Phys.* **5** 25–30

Ulmer W and Harder D 1996 Applications of a triple Gaussian pencil beam model for photon beam treatment planning *Z. Med. Phys.* **6** 68–74

Ulmer W, Pyyry J and Kaissl W 2005 A 3D photon superposition/convolution algorithm and its foundation on results of Monte Carlo calculations *Phys. Med. Biol.* **50** 1767–90

Van Esch A, Tillikainen L, Pyykkönen J, Tenhunen M, Helminen H, Siljamäki S, Alakuijala J, Paiusco M, Iori M and Huyskens D 2006 Testing of the analytical anisotropic algorithm for photon dose calculation *Med. Phys.* **33** 4130–48

Yang Y, Xing L, Boyer A L, Song Y and Hu Y 2002 A three-source model for the calculation of head scatter factors *Med. Phys.* **29** 2024–33